

## Supplemental Material

# Accelerated Transport through Sliding Dynamics of Rodlike Particles in Macromolecular Networks

Xuanyu Zhang,<sup>1,2</sup> Xiaobin Dai,<sup>1,2</sup> Md Ahsan Habib,<sup>3</sup> Lijuan Gao,<sup>1,2</sup> Wenlong Chen,<sup>1,2</sup> Wenjie Wei,<sup>1,2</sup> Zhongqiu Tang,<sup>3</sup> Xianyu Qi,<sup>4</sup> Xiangjun Gong,<sup>4</sup> Lingxiang Jiang,<sup>3,\*</sup> and Li-Tang Yan<sup>1,2,†</sup>

## CONTENTS

I. Details of Experiments of Rods in Macromolecular Networks and Simulations Pertinent to The Experiments	2
II. Details of Simulation Methods	4
III. Evaluation of The Distribution of Mesh Sizes	8
IV. A Theoretical Model of A Rod in The Macromolecular Network	9
V. Sliding and Hopping Dynamics of A Rod in The Macromolecular Network	10
VI. Rotational and Off-Axis Dynamics of A Rod in The Macromolecular Network	14
VII. Supporting Figures and Tables	16
References	23

## I. DETAILS OF EXPERIMENTS OF RODS IN MACROMOLECULAR NETWORKS AND SIMULATIONS PERTINENT TO THE EXPERIMENTS

*Preparation of samples of synthetic networks and rods.* The experimental network is polyethylene glycol diacrylate (PEGDA) network, which possesses excellent biocompatibility [1]. PEGDA network was prepared under UV irradiation [2]. 4% wt/vol solution of PEGDA (20 kDa, JenKem Technology USA) was prepared in distilled water and 0.02 g/ml lithium phenyl-2,4,6-trimethylbenzoylphosphinate (LAP) photo initiator was added. The solution was vortexed vigorously (Model: XH-D, Brand: Zigui, Shanghai), and then degassed by centrifuging (Model: TG16-WS, Brand: Cence, China) at 320 rpm for 5 min. The solution was cast on a 40 nm × 20 nm × 2 nm silicone slide with holes and cured under the UV light (wavelength 365 nm, 30 W) for 10 min. After the curing process, the PEGDA network was immersed under the distilled water for 48 h to remove the unreacted PEGDA monomers and allow the network to swell sufficiently. To calculate the mesh size of the network, we applied the methods developed by Peppas et al. [3, 4], which has been widely used in designing macromolecular network systems as drug carrier [5] and artificial cytoskeleton [6]. The averaged mesh size of the PEGDA network was determined to be around 21.0 nm. With regard to the rods, PEG-capped Au nanorods (Au-NR) with the same diameter but different lengths were purchased from NanoSeedz Limited, Hong Kong and used for diffusion experiments without any modification. For monodispersing of the Au-NR in water, Au-NR solutions were sonicated (Model: 2800, Brand: Branson, China) for 20 min prior to put on the microscopic slide. To obtain the diameter and length of Au-NRs, around 2.5  $\mu$ L Au-NR sample was first diluted by dissolving in around 0.2 mL ethanol, sonicated for at least 20 min, and then dropped 3-6  $\mu$ L solution on the transmission electron microscopy (TEM) copper grid. The copper grids were then stored at room temperature for at least 2 h to evaporate any solvent on it. Au-NR sizes were measured from the TEM images [Fig. S2] by Fiji(ImageJ) software, and the averaged values of rod lengths used in the entire experiments are listed in Table S2. The diameter of these rods, including the surface chemistry with a small thickness of 3.5nm, was estimated to be around 19.1 nm.

*Determination of trajectories of Au-NRs in the synthetic network.* To determine the trajectories of Au-NR in PEGDA network, we filled the network with 30  $\mu$ L Au-NR solution, which was kept for 10-15 min on an optical microscope stage (Olympus BX51) at room

temperature before observing the Au-NR diffusion into the PEGDA network [7]. For the trajectories of Au-NR in water, the microscopic slides were prepared almost in the similar way as mentioned above, but were filled with distilled water. The prepared slide was then kept on the microscope slides for at least 30 min before observing the trajectories. For analyzing the trajectories of Au-NR in both water and network, the images were taken by using dark field techniques [8]. For the water medium 400 images were recorded at a frequency of 20 Hz for 20 s time. On the other hand, for the hydrogel medium, total images were taken at a frequency of 10 Hz [9]. The general period for the measurement is 600s. However, to give the experimental DPDFs with enough statistical significance, an extended observation time up to 10800s, ensuring that at least 10 hopping events occur for the corresponding sample, was adopted for the calculation of DPDFs. The spots were then detected and trajectories were obtained by the Trackpy softwares [10]. Briefly, the images were first loaded on the Fiji (ImageJ) software [11] and adjusted the brightness and contrast for better observation of the particles. To detect the particiles in the image stack, filter-based method was used [12]. Particles trajectories were then obtained by Nearest Neighbor Search tracker, as shown in Fig. S3. To eliminate the experimental error due to the cumulative vibration and drift of the microscope stage used for imaging during a long-time measurement, we compute the overall drifting motion, which will be subtracted away, adopting the reference frame of the particles' average position; this method can significantly reduce the creeping movement of the microscope and has been widely used elsewhere [13–15]. The tracking data was then exported in a CSV file format, and time-averaged MSDs, ensemble-averaged MSDs and diffusion coefficients were calculated, as shown in Figs. S5, 1(b) and 1(c), respectively.

*Determination of the mesh size of PEGDA hydrogel.* To calculate the mesh size of the hydrogel, we applied the Canal-Peppas mesh size model [3, 4], which had been widely used in designing hydrogel systems as drug carrier [5] and artificial cytoskeleton [6]. According to this model, the mesh size can be calculated by using hydrogel swelling ratio  $Q$  and modulus  $G$ . In order to obtain the swelling ratio of PEGDA hydrogel, 0.8 ml PEGDA solution with photo initiator was cast in a 35 mm petri dish and UV cured to get around 15 mm thickness of hydrogel. Then the hydrogel was carefully pill-off from the petri dish, rinsed in water and transferred to a large petri dish. After that the hydrogel was cut into a 25 mm circular size with a stainless still dice, and immersed in the deionized water for 48 h to measure the

weight of the gel at swelling state ( $m_{swollen}$ ). It should be noted that, during the swelling experiment water was replaced with the fresh water in every 12 h. Then the same hydrogel sample was slowly dried in a dryer to get dry weigh of gel ( $m_{dry}$ ). Here, we obtained the volume of the swollen network  $V_{swollen}$ , the volume of the dry network  $V_{dry}$ , the actual (not swollen) density of the PEG  $\rho = 1.12$  g/mL, and the density of the water  $\rho_s = 18$  g/mL. Volumetric swelling ratio can be calculated based on below equation:

$$Q = \frac{V_{swollen}}{V_{dry}} = \frac{m_{dry}/\rho + (m_{swollen} - m_{dry})/\rho_s}{m_{dry}/\rho} = 43.7 \quad (\text{S1})$$

Rheology test for as-prepared PEGDA hydrogel was performed on a rotational rheometer (ARES G2, TA Instruments, USA) at 25°C. Five different samples were measured to determine storage modulus  $G'$  and loss modulus  $G''$ . The complex shear modulus  $G^* = G' + iG''$ , but as the viscous contribution was negligible, shear modulus for all of samples were calculated by using  $G = \sqrt{(|G'|^2 + |G''|^2)}$ . In detail, a parallel plate geometry of 20 mm diameter (PP 20) was used. As-prepared hydrogel cylinders were fixed between the plates.  $G$  was measured at an amplitude set within the linear elastic regime at constant frequency set to 1 Hz, and strain set to 1%. Based on  $G$ , the swelling ratio  $Q$  and a characteristic constant  $C_n$ , we estimated a theoretical mesh size by using the following equation [3]:

$$\langle\xi\rangle_G = l \sqrt{\frac{RT C_n \rho}{x M_r G Q}} \quad (\text{S2})$$

where  $x$  is the number of binding for each chain (2 in case of PEGDA used in the experiments),  $\rho$  is the actual (not swollen) density of the repeating unit of the PEG, and  $M_r$  is the molar weight of the monomer (44g/mol).  $C_n$  is a characteristic constant (usually  $C_n \approx 4$ ), and  $l$  is the distance between C-C backbone,  $l \approx 0.154 \times 2$  nm for PEG.  $RT$  (kPa · mol<sup>-1</sup>) at absolute temperature and is obtained from the universal gas constant,  $R$ . The calculation results are shown in Table S3.

## II. DETAILS OF SIMULATION METHODS

In this paper, the transport of a rodlike particle in the macromolecular network is modeled by dissipative particle dynamics which is a coarse-grained molecular simulation method [16] and has been successfully used to model the structural and dynamic properties of macromolecular networks [17–19]. In the simulations, a bead represents a cluster of molecules,

and a set of interacting beads are considered. The time evolution is governed by Newton's equations of motion,  $(m d\mathbf{v}_i)/dt = \mathbf{f}_i$ . The force contains three parts, each of which is pairwise additive:  $\mathbf{f}_i = \sum (\mathbf{F}_{ij}^C + \mathbf{F}_{ij}^D + \mathbf{F}_{ij}^R)$ , where the sum runs over all beads  $j$  within a certain cutoff radius  $r_c$ . The conservative force is a repulsion acting along the line of bead centers, which is given by  $\mathbf{F}_{ij}^C = a_{ij} (1 - r_{ij}) \hat{\mathbf{r}}_{ij}$ , where  $\mathbf{r}_{ij} = \mathbf{r}_i - \mathbf{r}_j$ , and  $\hat{\mathbf{r}}_{ij} = \mathbf{r}_{ij}/|\mathbf{r}_{ij}|$ .  $a_{ij}$  is a maximum repulsion between bead  $i$  and bead  $j$ . The interaction between like species  $a_{ii}$  is set as 25 [16]. To bring out the entropic nature of the interplay between rods and network strands, in this study, the rod-strand interaction  $a_{rp}$  is set to be the same as that between like beads, resembling the rods in the  $\theta$ -solvent of network strands where screened excluded-volume statistics can be assumed [20]. The dissipative force and random force are given by  $\mathbf{F}_{ij}^D = -\gamma \omega_D(r_{ij}) (\hat{\mathbf{r}}_{ij} \cdot \mathbf{v}_{ij}) \hat{\mathbf{r}}_{ij}$  and  $\mathbf{F}_{ij}^R = \sigma \omega_R(r_{ij}) \theta_{ij} \hat{\mathbf{r}}_{ij}$ , where  $\omega_D$  and  $\omega_R$  are  $\mathbf{r}$ -dependent weight functions and  $\mathbf{v}_{ij} = \mathbf{v}_i - \mathbf{v}_j$ .  $\gamma$  is a simulation parameter related to the viscosity arising from the interactions between the beads and  $\sigma^2 = 2k_B T \gamma$ , where  $k_B$  is the Boltzmann constant and  $T$  is the temperature.  $\theta_{ij}$  is a zero-mean Gaussian random variable of unit variance. These forces also act along the line of centers and conserve linear and angular momentum. Thus we use  $\omega_D(r_{ij}) = \omega_R(r_{ij})^2 = (1 - r_{ij})^2$  for  $r_{ij} < 1$ . Since all of these forces conserve momentum locally, hydrodynamic behavior emerges. The equations of motion are integrated in time with a modified velocity-Verlet algorithm. The factor  $k_B T$  is taken as the characteristic energy scale. In our simulations,  $k_B T = 1$ . The characteristic time scale is then defined as  $\tau = (mr_c^2/k_B T)^{1/2} = 1$ . The remaining simulation parameters are  $\gamma = 4.5$  and  $\Delta t = 0.02\tau$  with a total bead number density of  $\rho = 3$ . The total simulation time is set as  $t = 8 \times 10^4 \tau$  which is long enough that mean square displacement (MSD) converges to linear dependence on time in logarithmic relationship.

To demonstrate the dynamics of a rod-like particle in the network, we choose a cubic box with dimensions of  $42.76r_c \times 42.76r_c \times 42.76r_c$ . The configuration of a network is taken to be a hexa-functional network, with periodic boundary condition in all directions. Such a network in this study consists of 46137 bonds and 2197 cross-links. Although mesh size of the network model is monodispersed, after a quantitative evaluation of the effects of the mesh size distribution on the dynamical behaviors as detailed in Section III of this Supplemental Material, we find that the nonmonotonic dependence of the diffusivity on  $L$  for thick rods still keeps in relatively broad distribution of the mesh size, indicating that the dynamical behaviors in the network within a certain scope of polydispersity can still fall

into the physical principle revealed based on the regular network. Indeed, the simulation results based on this network capture the experimental results very well, as shown in Fig. 1(c).

A general particle-building model is adopted to build a set of rod particles fabricated by numbers of beads [21], and the rods move as rigid bodies with the Quaternion scheme [22], which is widely used in the simulations of the motion of rigid body and has been fully demonstrated to faithfully capture the transport of the nanoparticles [23]. Specifically, the rods are modeled as clusters of monomer sized beads, which have a diameter of  $0.6r_c$ . The rod is fabricated by arranging the beads on a triangulation surface with the inter-particle distance of  $0.4r_c$ , ensuring that the rod is not penetrated by other beads. By combining the linear and rotational physics into a single physics state and integrating, the motion of a rigid body in three dimensions can be simulated. The rod is originally located at the center of box and the principal axis of the rod is initially aligned parallel to the **z**-axis, as indicated in Fig. 1(a). The network mesh size  $a_x$ , being essentially the correlation length between all pairs of strands comprising the networks [Fig. 1(a)], is fixed at about  $a_x = 3.35r_c$ . Particularly,  $d$  is set to be comparable to the mesh size, ranging from  $1.3a_x$  to  $1.9a_x$ , and  $L$  ranges from  $1.5a_x$  to  $4.4a_x$ , with which the off-axis dynamics is negligible (see Section VI for more details). The normalized sizes  $d/a_x$  and  $L/a_x$  are used, representing the size matching between a rod and a network mesh.

To evaluate effectiveness of the simulation model in the present systems, we perform calculation based on the specific experiments and compare our simulation outcome directly with the experimental results. Specifically, the experimental system is selected as a nanorod with  $d = 20\text{nm}$  and  $L = 40\text{ nm}$  in the PEGDA network. We relate the simulation parameters of physical length and time scales through the values of the collective diffusion coefficient of the rod [17]. The length  $r_c$  can be considered as the side of a cube containing an averaged of  $\rho$  beads [24]. Therefore,  $r_c = (\rho V_b)^{1/3}$ , where  $V_b$  is the volume of a bead. From Ref. [25], we choose the sizes of the rod as  $d = 20\text{ nm}$  and  $L = 40\text{ nm}$ , and the rod consists of 251 beads in our simulations. Thus, the volume of the rod  $V_r = \pi d^2 L / 4 = 1.26 \times 10^4\text{ nm}^3$ , and  $V_b$  is around  $50.2\text{ nm}^3$ . Because the bead density  $\rho$  is 3, a cube of  $r_c^3$  contains three beads and therefore corresponds to a volume of  $158\text{nm}^3$ . Thus, the physical size of the interaction radius,  $r_c$ , is estimated as  $5.32\text{ nm}$ .

To measure the viscosity of our experimental systems, i.e., nanorod in the polymer solu-

tion, by performing additional particle tracking experiments of this nanorod in 4% PEGDA solution. The rod is considered as an equivalent sphere in the follow calculation, and thus the hydrodynamic diameter of the rod can be estimated as  $r_h = (3Lr^2/4)^{1/3} = 22.9\text{nm}$ . As shown in Fig. S9, the MSD of the nanorod in the polymer solution exhibits the normal diffusion, with diffusion exponent 1 as expected at all time scale. Using a linear regression in log space, we can easily fit this ensemble MSD to a power law,  $\langle \Delta r^2 \rangle = At$ , where  $A = 0.0295\mu\text{m}^2/\text{s}$ . For 2-dimensional diffusion in the particle tracking experiment, the diffusion coefficient of the nanorod can be calculated as  $D_{exp} = A/4 = 0.0737\mu\text{m}^2$ . Using the Stokes-Einstein (SE) equation,  $D_{exp} = k_B T / (6\pi\mu r_h)$ , we can calculate the real viscosity of the nanorod,

$$\mu = \frac{k_B T}{6\pi D_{exp} r_h} = 1.32\text{Pa}\cdot\text{s} \quad (\text{S3})$$

To further corroborate that our model captures the entropic nature arisen by the larger diameters of bacterium, we perform simulations by setting  $d/a_x$  a typical value in Fig. S10 but a range of particle-strand interaction parameters corresponding to various enthalpic contributions. As shown in Fig. S10, the speeding-up longitudinal dynamics still occurs once the rod length reaches around integral multiple of  $a_x$  for both attractive ( $a_{ij} < 25$ ) and repulsive ( $a_{ij} > 25$ ) particle-strand interactions, which obeys the same laws as the case mentioned in the main text, underscoring that the entropic contribution does dominate the behaviors.

*Simulations pertinent to the experiments.* In these simulations, the box is still with dimensions of  $42.76r_c \times 42.76r_c \times 42.76r_c$ . The configuration of a network is taken to be a hexa-functional network, with  $a_x = 3.35r_c$ . Such a network in this study consists of 46137 bonds and 2197 cross-links. A general particle building model is adopted to build a set of rod particles fabricated by numbers of beads [21], and the rods move as rigid bodies with the Quaternion scheme [22]. In order to make it pertinent to the experiments,  $d/a_x$  is set as 1.05 and a set of  $L/a_x$  are selected as 1.5, 2.0, 2.2, 2.5 and 3.0. We perform the simulations both in the network and neat solvent to get a set of  $D$  and  $D_0$ , where  $D$  is the longtime diffusion coefficient in the network and  $D_0$  denotes that in neat solvent. To ensure that the experiments and the simulations are comparable, we compare the normalized diffusion coefficients of them,  $D/D_0$ , which are illustrated in Fig. 1(c).

### III. EVALUATION OF THE DISTRIBUTION OF MESH SIZES

Generally, there is a distribution of mesh sizes in a real network, leading to the polydispersity of molecular structures of the network. In fact, this important factor is evaluated carefully through quantifying the distribution of mesh sizes of some typical biological networks and further examining the speeding-up dynamics of thick rods in them. We find that, within the typical range of mesh size distribution of these biological networks, it actually plays a trivial role in the dynamical behaviors of such *thick* rods, and the rod-length dependent speeding-up dynamics remains.

Specifically, we have quantified the distribution of mesh sizes through calculating the coefficient of variation of mesh sizes, defined as  $CV = \sigma_{a_x}/a_x$ , of some typical biological networks, where  $\sigma_{a_x}$  is the standard deviation of mesh sizes. To realize this goal, we performed a careful literature survey and thereby obtained the estimation regarding that the CV of typical biological mucus approximately ranges from 0.1 to 0.8. For instance, the mesh size of 3.0g/L collagen gel is almost monodisperse with  $CV = 1 \mu\text{m} / 7 \mu\text{m} \approx 0.14$  [26]; in human cervicovaginal mucus, the pore size was measured, giving a narrow distribution with  $CV = 70 \text{ nm} / 340 \text{ nm} \approx 0.21$  [27]; in rat intestinal mucus,  $CV = 93.18 \text{ nm} / 186 \text{ nm} \approx 0.50$  [25]; the mesh size of human cervical mucus is highly disperse with  $CV = 0.7 \mu\text{m} / 0.9 \mu\text{m} \approx 0.78$  [28].

Further, to examine how the distribution of networks affects the dynamical behaviors of the thick rods, we perform simulations to study the thick rod diffusion in the macromolecular network with a broad distribution of mesh sizes, demonstrating that the accelerated dynamics still occurs once the rod length reaches around integral multiple of  $a_x$ . Based on the analysis of CV in mucus, we set  $CV = 0.3, 0.7$  and  $0.8$  by varying the distribution of strand lengths in our simulations. As shown in Fig. S11(a) and (b), for  $d/a_x=1.4$ , the speeding-up dynamics indeed occurs when the rod length is commensurate with  $a_x$  at  $CV = 0.3$  and  $0.7$ . Even at  $CV = 0.8$ , although the speeding-up diffusion is not much evident for the commensurate rods of  $d/a_x = 1.4$ , the speeding-up dynamics emerges again for the thicker rods with  $d/a_x = 1.5$ , indicating that the thicker the rod, the wider pore size distribution permitted. Nevertheless, the simulation results of the macromolecular networks, whose polydispersity approximates to those of typical biological networks, can still fall to the physical principles revealed based on the regular network, underscoring that the neat

model can be applied to mimic the dynamical behaviors in mucus, especially for the thick rods concerned in our work.

#### IV. A THEORETICAL MODEL OF A ROD IN THE MACROMOLECULAR NETWORK

We start from the Deam-Edwards Hamiltonian of a Gaussian network with excluded volume of a rod [29],

$$H(\mathbf{R}_{ij}, \mathbf{r}_{rod}, \mathbf{l}_{rod}) = \frac{3k_B T}{2Nb^2} \int_0^1 ds \left( \frac{\partial \mathbf{R}_{ij}(s)}{\partial s} \right)^2 + U_{pm}(\mathbf{R}_{ij}, \mathbf{r}_{rod}, \mathbf{l}_{rod}) \quad (\text{S4})$$

where  $\mathbf{R}_{ij}(s)$  is the path vector of the strand with its start  $\mathbf{R}_{ij}(0) = \mathbf{r}_i$  and end  $\mathbf{R}_{ij}(1) = \mathbf{r}_j$ ,  $\mathbf{r}_{rod}$ ,  $\mathbf{l}_{rod}$  are the position and directional vectors of the rod,  $s \in [0, 1]$  is the contour variable,  $N$  is the number of bonds in a strand, and  $b$  is the Kuhn length. The hard-core interaction between the monomer and rod is given by,

$$U_{mr}(\mathbf{R}_{ij}, \mathbf{r}_{rod}, \mathbf{l}_{rod}) = \begin{cases} \infty & \|(\mathbf{R}_{ij} - \mathbf{r}_{rod}) \cdot \mathbf{l}_{rod}\| < L/2, \|(\mathbf{R}_{ij} - \mathbf{r}_{rod}) - (\mathbf{r}_{ij} - \mathbf{r}_{rod}) \cdot \mathbf{l}_{rod}\| < d/2 \\ 0 & \text{else} \end{cases} \quad (\text{S5})$$

where  $d$ ,  $L$  are the diameter and length of the particle, respectively. By substituting the equations below, we get the partition function of the entire system [30],

$$Z(\mathbf{r}_{rod}, \mathbf{l}_{rod}) = \prod_k \int d\mathbf{r}_k \prod_{(i,j)} \int \mathcal{D}\mathbf{R}_{ij} \delta(\mathbf{r}_i - \mathbf{R}_{ij}(0)) \delta(\mathbf{r}_j - \mathbf{R}_{ij}(1)) \exp[-\beta H(\mathbf{R}_{ij}, \mathbf{r}_{rod}, \mathbf{l}_{rod})] \quad (\text{S6})$$

where  $k = \{\mathbf{r}_i\}_{i=1}^M$  is the set of cross-links containing  $M$  cross-links between the efficiently bridged Gaussian chains, and  $(i, j)$  represents linker connections with ends  $\mathbf{r}_i$  and  $\mathbf{r}_j$ . The Helmholtz free energy of the system is given by,

$$F(\mathbf{r}_{rod}, \mathbf{l}_{rod}) = -k_B T \ln Z(\mathbf{r}_{rod}, \mathbf{l}_{rod}) \quad (\text{S7})$$

For Gaussian chains, the correlation function of  $\partial \mathbf{R}_{ij}(s)/\partial s$  gives,

$$\int ds \frac{\partial \mathbf{R}_{ij}(s)}{\partial s} \cdot \frac{\partial \mathbf{R}_{ij}(s')}{\partial s'} = \int ds \delta(s - s') \left\| \frac{\partial \mathbf{R}_{ij}(s)}{\partial s} \right\|^2 \quad (\text{S8})$$

We thereby define the integral of a strand,

$$\begin{aligned} L_{ij}(\mathbf{R}_{ij}, \mathbf{r}_{rod}, \mathbf{l}_{rod}) &= \int_0^1 ds \frac{\partial \mathbf{R}_{ij}(s)}{\partial s} \\ &\times \Phi(\|(\mathbf{R}_{ij} - \mathbf{r}_{rod}) \cdot \mathbf{l}_{rod}\| - L/2) \Phi(\|(\mathbf{R}_{ij} - \mathbf{r}_{rod}) - (\mathbf{R}_{ij} - \mathbf{r}_{rod}) \cdot \mathbf{l}_{rod}\| - d/2) \end{aligned} \quad (\text{S9})$$

where  $\Phi$  is the step function.

As shown in Fig. S12, to calculate the integral of a strand  $L_{ij}(\mathbf{R}_{ij}, \mathbf{r}_{rod}, \mathbf{l}_{rod})$  cross-linked by points  $P$  and  $Q$  at positional vectors  $\mathbf{r}_i$  and  $\mathbf{r}_j$ , we consider an osculating plane  $A$  (green plane) coming across the points  $P$ ,  $Q$  and  $O_0$  with the normal vector  $\mathbf{n}$ . The path of the chain  $\mathbf{R}_{ij}$  from  $P$  to  $Q$  in the plane  $A$  desires to be one of the conformations of chains  $\mathbf{R}_{ij}(s)$ . Randomly selecting the normal vector  $\mathbf{n}$  gives all conformations of chains that slip around the surface of rod. Here, the dihedral angle  $\theta$  is defined as,

$$\theta = \arccos \frac{\mathbf{n} \cdot \mathbf{l}_{rod}}{\|\mathbf{n}\| \|\mathbf{l}_{rod}\|} \quad (\text{S10})$$

so that the path integral  $\int \mathcal{D}\mathbf{R}_{ij} f(\mathbf{R}_{ij})$  can be converted to  $\int d\theta \int d\mathbf{n} g(\mathbf{R}_{ij}, \mathbf{n})$ , where  $f$  and  $g$  are functions.

In the calculations, we apply the Graham scan algorithm [31] on the convex shape of the “untouched” area to evaluate the integral length  $L_{ij}(\mathbf{R}_{ij}, \mathbf{r}_{rod}, \mathbf{l}_{rod})$  of path  $\mathbf{R}_{ij}$  for various  $\mathbf{n}$ . Here, we study the condition that the strand contacts the surface of the rod. Its solution can be written as

$$\begin{cases} \|\mathbf{(r - r_{rod})} \cdot \mathbf{l}_{rod}\| < L/2 \\ \|\mathbf{r - r_{rod}} - \mathbf{(r - r_{rod})} \cdot \mathbf{l}_{rod}\| < d/2 \end{cases} \quad (\text{S11})$$

where  $\mathbf{r} = \lambda \mathbf{r}_p + (1 - \lambda) \mathbf{r}_q$  represents the points on line segment  $PQ$ , and  $0 \leq \lambda \leq 1$ . If contacts, the integral  $L_{ij}$  is determined by the intersection of the convex shape in plane  $A$ , taking the form

$$\begin{cases} \|\mathbf{(r - r_{rod})} \cdot \mathbf{l}_{rod}\| < L/2 \\ \|\mathbf{r - r_{rod}} - \mathbf{(r - r_{rod})} \cdot \mathbf{l}_{rod}\| < d/2 \\ \|\mathbf{(r - r_{rod})} \cdot \mathbf{n}\| = 0 \end{cases} \quad (\text{S12})$$

## V. SLIDING AND HOPPING DYNAMICS OF A ROD IN THE MACROMOLECULAR NETWORK

In this section, we provide a more detailed discussion regarding the dynamical regimes of Brownian, sliding, and hopping dynamics for a rod in the macromolecular network. If  $n$  jumps have occurred up to time  $t$ , the distribution of the total number of the network cells traversed can accordingly be obtained in Fourier-Laplace space from the Montroll-Weiss

equation [32],

$$S(k, s) = \frac{1 - \tilde{\psi}(s)}{s \left[ 1 - \hat{\phi}(k) \tilde{\psi}(s) \right]} \quad (\text{S13})$$

where  $\tilde{\psi}(s)$  is the Laplace transform of the waiting time distribution  $\psi(t)$  and  $\hat{\phi}(k)$  is the Fourier transform of the hopping length distribution  $\phi(\tilde{z})$ .

The waiting distribution  $\psi(t)$  can be established on the basis of the long time asymptotic behaviour of the rod. Since the mean square displacements (MSD) of Brownian, sliding, and hopping dynamics recover back to the normal diffusion in the long-time scale in Fig. 2(a), it can be approximated that the waiting process is a Poisson process [33]. The waiting time distribution of Poisson process in continuous time domain take the exponential form, which is given by

$$\psi(t) = \frac{1}{\tau_{hop}} \exp\left(-\frac{t}{\tau_{hop}}\right) \quad (\text{S14})$$

In terms of Kramers' rate theory [34], the well-separation time scales can be obtained and the averaged time of the waiting process can be described as,

$$\tau_{hop} = \frac{2\pi\gamma}{\sqrt{|k_s|k_l}} \exp(U_b/k_B T) \quad (\text{S15})$$

where  $k_s$  and  $k_l$  are the curvatures of the potential along  $\mathbf{z}$ -axis at the saddle point  $\tilde{z} = 0$  and the starting minimum  $\tilde{z} = 0.5a_x$ , respectively.

The jumping length distribution  $\phi(\tilde{z})$  relies on the free energy barrier  $U_b$  in different regimes, as discussed below:

(1) For the hopping dynamics, the particle spends most of the time close to the minimum free energy point in a network cell and only occasionally escapes to another one. It can be estimated that the hopping length is the integral multiple of the mesh size  $a_x$  with regard to the periodic conditions, and thus  $\phi(\tilde{z})$  has the periodic distribution [35, 36]

$$\phi(\tilde{z}) = NP(n)\delta(|\tilde{z}| - na_x) \quad (\text{S16})$$

where  $a_x$  is the characteristic hopping length,  $P(y) = \exp(-4\beta U_b y^2/a_x^2)$  gives the Boltzmann distribution,  $U_b$  represents the energy barrier,  $n$  is an integral number, and  $N$  is the normalization constant such that  $\sum_{n=0}^{\infty} NP(na_x) = 1$ . By subtracting the Laplace transformation of Eq. (S14)  $\tilde{\psi}(s) = 1/(1 + \tau_{hop}s)$  and performing the inverse Laplace transformation of Eq. (S13), we can get the characteristic function  $K(k, t)$  in the time domain,

$$K(k, t) = \exp \left\{ -\frac{t}{\tau_{hop}} \left[ 1 - \hat{\phi}(k) \right] \right\} \quad (\text{S17})$$

For short time scales,  $t \ll \tau_{hop}$ , the hopping event doesn't happen, so that Eq. (S16) can be assumed by,  $\phi(\tilde{z}) = NP(\tilde{z})\delta(\tilde{z})$ . Substituting the Laplace transformation of that, it can be obtained by the first-order approximation,

$$K(k, t) = 1 - \frac{t}{\tau_{hop}} \left[ 1 - \exp \left( -\frac{k^2}{4\beta U_b/a_x^2} \right) \right] \quad (\text{S18})$$

As a result, in position space we obtain

$$G_s(\tilde{z}, t) = \delta(\tilde{z}) \left( 1 - \frac{t}{\tau_{hop}} \right) + \frac{t}{\tau_{hop}} \frac{a_x}{2\sqrt{2\pi\beta U_b}} \exp \left( -\frac{\tilde{z}^2}{16\pi\beta U_b/a_x^2} \right) \quad (\text{S19})$$

In contrast, for long time scales,  $t \gg \tau_0$ , we perform saddle-point approximations around  $k = 2\pi/a_x, \pi/a_x, 2\pi/3a_x, \dots$ , and yields

$$K(k, t) = \exp \left[ -\frac{t}{\tau_{hop}} k^2 a_x^2 \right] \quad (\text{S20})$$

where the aliased characteristic function  $K$  is defined on the interval  $(-\pi/a_x, \pi/a_x]$  [36]. The displacement distribution  $G_s(\tilde{z}, t)$  is thus evaluated by the convolution in each interval

$$G_s(\tilde{z}, t) = \sum_{n=0}^{\infty} NP(n) \delta(|\tilde{z}| - na_x) \frac{1}{\sqrt{4\pi a_x^2 \frac{t}{\tau_{hop}}}} \exp \left[ -\frac{x^2}{4 \frac{t}{\tau_{hop}} a_x^2} \right] \quad (\text{S21})$$

(2) For the sliding dynamics, to describe the non-local nature of irregular peaks in  $G_s(\tilde{z}, t)$ , we apply the master equation for the random walk, which is given by

$$G_s(\tilde{z}, t) = G_s(\tilde{z}, 0) + \int_0^t \sum_{\tilde{z}'} \omega(\tilde{z} - \tilde{z}') G_s(\tilde{z}', t') dt \quad (\text{S22})$$

where  $\omega(\tilde{z})$  is the kernel of the diffusion equation. Eq. (S22) can be transformed into the discrete form,

$$G_s(\tilde{z}, t) = \sum_{n=0}^{\infty} P(n, t) P(\tilde{z}, n) \quad (\text{S23})$$

where  $P(\tilde{z}, n)$  and  $P(n, t)$  represent the probability density function (PDF) of the displacement and the number of hopping events happened.

We consider that at time  $t$ , the random variable of displacement  $X_t$  gives

$$X_t = \sum_{k=0}^{\infty} J_k \quad (\text{S24})$$

where  $J_k$  is the jump length with its distribution  $\phi(\tilde{z})$ . Each jump can be seemed as a difference of two independent variables  $J_k = J_k^+ - J_k^-$ , where  $J_k^+$ ,  $J_k^-$  denote forward and backward

displacements between two neighboring cells with the same distance  $L$ . According to the Poisson point measure [37], the probability of the distance between any two consecutive cells on this line is exponential, given by

$$p(L) = \frac{1}{a_x} \exp\left(-\frac{L}{a_x}\right) \quad (\text{S25})$$

For a given cell with a fixed  $L$ , the distribution is uniform. In one dimension, it is  $p(z|L) = 1/L$ ,  $|z| < L/2$ , yielding,

$$\phi(\tilde{z}) = \int_{|z| < L/2} p(L)p(\tilde{z}|L)dL = \frac{1}{a_x} \exp\left(-\frac{2|\tilde{z}|}{a_x}\right) \quad (\text{S26})$$

which is found to be the Laplace (also called “two sided exponential”) distribution with mean 0 and variance  $a_x/2$ , written as  $J_k \sim \text{Lap}(0, a_x/2)$ .

Then two compound Poisson processes  $N_t^+ = \{T_1 + T_2 + \dots + T_k, J_k^+\}$ ,  $N_t^- = \{T_1 + T_2 + \dots + T_k, J_k^-\}$  for the independent waiting time spans  $T_k$  are obtained, where  $T_k \sim \text{Poiss}(2t/\tau_{hop})$  gives the standard Poisson distribution. We may thereby represent the total displacements as a difference of two positive independent processes,  $X_t = X_t^+ - X_t^-$ , where  $X_t^\pm = \sum_{k=0}^{N_t^\pm} J_k^\pm$ .

It can be proved that the sum of independent exponential distribution gives Gamma distribution, i.e.,  $\sum_{k=0}^n J_k^\pm \sim \text{Gamma}(n + 1, 2/a_x)$ . By substituting the PDF Poisson distribution  $P_{N^\pm}(n, t) = \frac{(t/\tau_{hop})^n}{n!} \exp(-\frac{t}{\tau_{hop}})$  and the Gamma distribution  $P_{X^\pm}(\tilde{z}, n) = \frac{(2\tilde{z}/a_x)^n}{n!} \exp(-\frac{2\tilde{z}}{a_x})$ , the PDF of  $X_t^\pm$  gives,

$$\begin{aligned} P_{X^\pm}(\tilde{z}, t) &= \sum_{n=0}^{\infty} P_{N^\pm}(n, t) P_{X^\pm}(\tilde{z}, n) \\ &= 2 \sum_{n=0}^{\infty} \left[ \frac{(2\tilde{z}t/a_x\tau_{hop})^n}{(n!)^2} \right] e^{-2\frac{\tilde{z}}{a_x}} e^{\frac{t}{\tau_{hop}}} \\ &= 2I_0\left(2\sqrt{2\tilde{z}t/a_x\tau_{hop}}\right) e^{-2\frac{\tilde{z}}{a_x}} e^{\frac{t}{\tau_{hop}}} \end{aligned} \quad (\text{S27})$$

where  $I_0$  is the modified Bessel function of the first kind. The PDF of  $X_t$  takes the convolution of Eq.(S27),

$$\begin{aligned} G_s(\tilde{z}, t) &= \int_0^\infty dx P_{X^+}(x + |\tilde{z}|, t) P_{X^-}(x, t) \\ &= 4e^{\frac{-2|\tilde{z}|}{a_x}} e^{\frac{-2t}{\tau_{hop}}} \int_0^\infty dx e^{-4x/a_x} I_0\left(\sqrt{\frac{8t(|\tilde{z}| + x)}{a_x\tau_{hop}}}\right) I_0\left(\sqrt{\frac{8tx}{a_x\tau_{hop}}}\right) \end{aligned} \quad (\text{S28})$$

(3) For the Brownian dynamics with  $U_b=0$ , the jump length takes the form of Gaussian distribution,

$$\phi(\tilde{z}) = \frac{1}{\sqrt{4\pi a_x}} \exp\left(-\frac{\tilde{z}^2}{4a_x^2}\right) \quad (\text{S29})$$

which exhibits normal diffusion at all times. Substituting Eqs. (S14) and (S29) into Eq. (S13), and taking the inverse Fourier-Laplace transformation, we get

$$G_s(\tilde{z}, t) = \frac{1}{\sqrt{4\pi a_x^2 \frac{t}{\tau_0}}} \exp\left(-\frac{\tilde{z}^2}{4a_x^2 \frac{t}{\tau_0}}\right) \quad (\text{S30})$$

where  $\tau_0$  is the characteristic waiting time in solvents.

## VI. ROTATIONAL AND OFF-AXIS DYNAMICS OF A ROD IN THE MACROMOLECULAR NETWORK

The rotation and off-axis dynamics of a rod significantly depend on its length as well as diameter[38–40]. To consider this issue, we first provide a strict examination of the simulation and experimental results regarding the rotational dynamics of the long and thick rods used in the present work. Within the whole temporal scales (over 600s) of simulation and experiments, almost no motion towards the direction normal to the z-axis can be identified, indicating that within the ranges of rod length and diameter in the present work, the rotational event takes place in an extremely low probability and thereby has little effect on the longitudinal motion of the rods in the macromolecular networks.

Next, we provide a fundamental discussion on the rotational and off-axis dynamics of a rod, through theoretically calculating the free energy barrier for the rod rotation in the macromolecular network and thereby estimating the waiting time for a rotational event. Theoretically, due to the confinement of the network strands, the rod should surmount an energy barrier when rotating in the network. Based on the theoretical model of a rod in the macromolecular network, as stated in the above section, we calculate the rotational energy barrier contributed by the local network strands, i.e.,  $\Delta E_{rot} = \Delta F_{max} - \Delta F_{min}$  , where  $\Delta F_{max}$  and  $\Delta F_{min}$  denote respectively the maximum and minimum free energy in all the rod directions characterized by the parameter  $\mathbf{l}_{rod}$  in Eqs.(S4–S7). The results indicate that the longer and thicker of a rod, the higher energy it experiences when rotating, and for a typical rod used in the current work, with diameter  $d/a_x = 1.0$  and length  $L/a_x = 2.0$ ,

the energy barrier can be calculated as  $10.3 k_B T$ . Furthermore, the waiting time for the rotational event can be determined by the Kramers' rate theory [34],

$$t_{hop} = t_{r0} \exp(\Delta E_{rot}/k_B T) \quad (\text{S31})$$

where  $t_{r0}$  is the waiting time for rotating at  $\Delta E_{rot} = 0$  and can be estimated in polymer solution. The rotational diffusion coefficient of the rod of  $d/a_x = 1.0$  and length  $L/a_x = 2.0$  in polymer solution can be calculated as

$$D_r = \frac{k_B T}{8\pi\mu r_h^3} = 10.03 \text{s}^{-1} \quad (\text{S32})$$

where the solvent viscosity is  $\mu = 1.32 \text{Pa} \cdot \text{s}$  and the hydrodynamic radius  $r_h = 22.9 \text{nm}$  (see Section II of Supplemental Material for more details). Thus, the waiting time in the pure solvent can be obtained, as  $t_{r0} = 1/D_r = 0.0997 \text{s}$ . Then, with Eq. (S31), the waiting time at  $\Delta E_{rot} = 10.3 k_B T$  is realized, as

$$t_{hop} = 2.96 \times 10^3 \text{s} \quad (\text{S33})$$

which is much larger than the observation time in experiment (600s). Actually, almost all the rod lengths used in our experiments are equal or even larger than  $L = 40 \text{nm}$ , indicating that the rotational dynamics does play a trivial role in the transport of nanorods in these systems. Note that the only one exception is the rod with  $L = 30 \text{nm}$  ( $L/a_x = 1.5$ ) and the calculation of  $t_r$  for this system is about 200 s. Although this value is a little smaller, the rotational event take place in a low probability if considering the observation time of 600s, which, we believe, has a little effect on the longitudinal motion of this rod in the macromolecular network and cannot modify the physics of the whole experimental systems.

## VII. SUPPORTING FIGURES AND TABLES

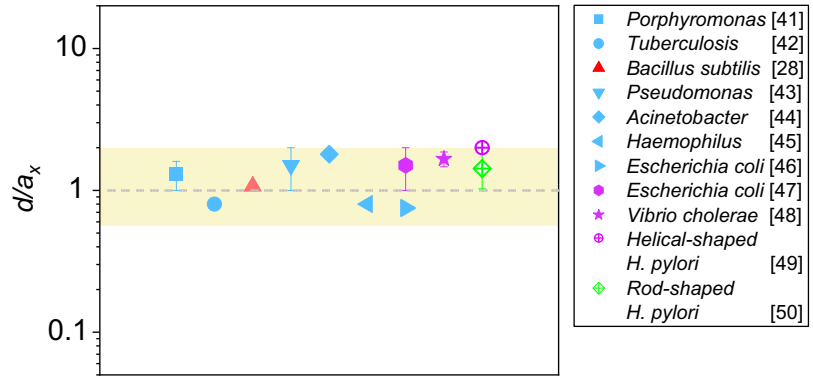


FIG. S1.  $d/a_x$  for some recent demonstrations of various bacteria in different mucus. Each point with the same shape and color represent the same system in both panels. The point shape denotes bacterial type, as given in the panels. The color represents mucus type: (cyan) human airway mucus [41–46], (light red) cow cervical mucus [28], (purple) human gastrointestinal mucus [47–49], (green) porcine gastric mucus [50]. More detailed information is listed in Table. S1.

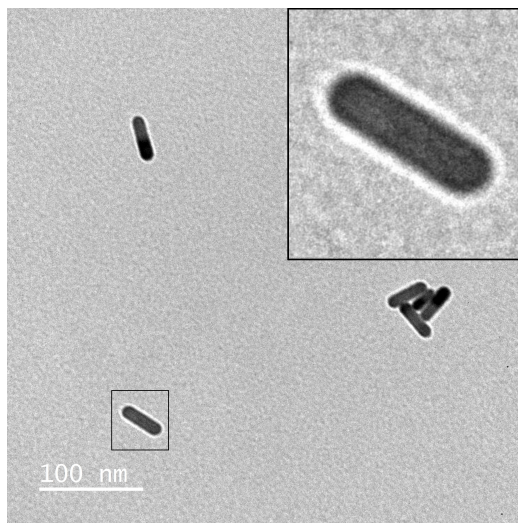


FIG. S2. A TEM image showing the representative Au-NRs used in experiments, where the length and diameter of the rod are  $52.5 \pm 5.6\text{nm}$  and  $19.6 \pm 1.7\text{ nm}$ , respectively. The inset shows a rod with enlarged size, highlighting the grafted layer, where the side length of the box is 50nm.

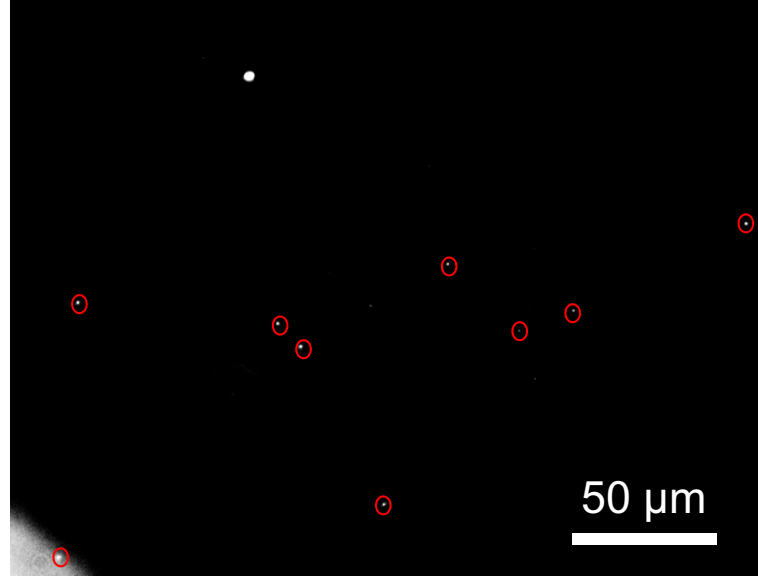


FIG. S3. A typical snapshot of rods in macromolecular networks in dark field microscopy, where the averaged length of rods is around 30.6 nm. The position of each rod is marked by a red circle.

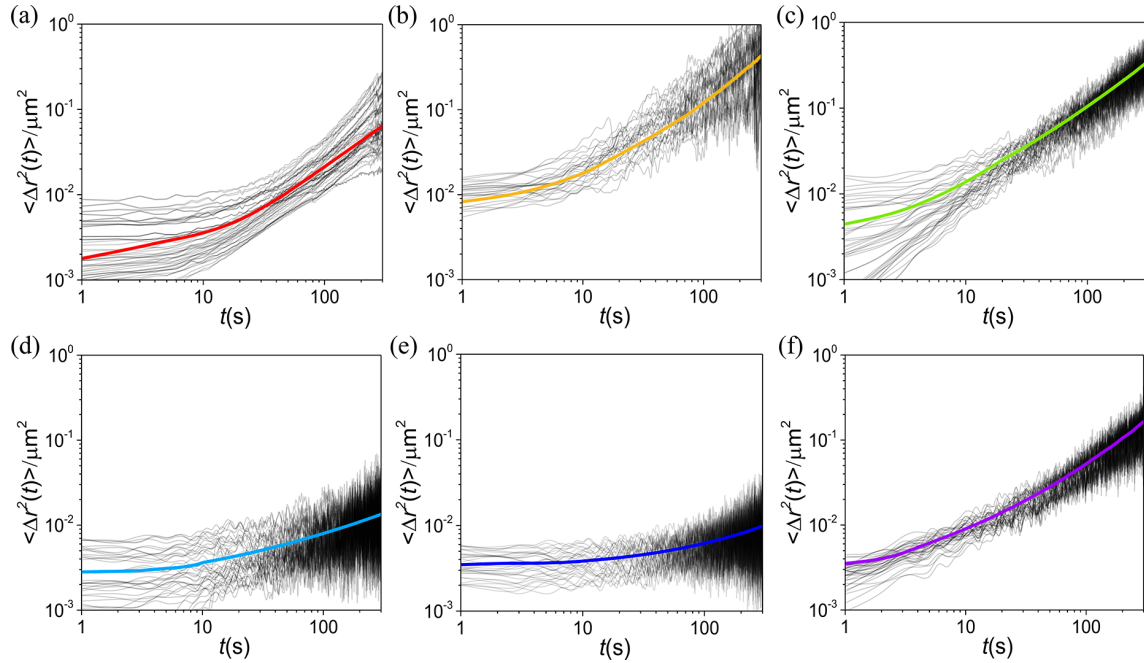


FIG. S4. Time-averaged (gray lines) and ensemble-averaged (colored lines)  $\langle \Delta r^2(t) \rangle$  plotted against time on log-log scales at different  $L/a_x$ : (a)  $L/a_x = 1.46 \pm 0.16$ , (b)  $L/a_x = 2.02 \pm 0.18$ , (c)  $L/a_x = 2.16 \pm 0.24$ , (d)  $L/a_x = 2.51 \pm 0.27$ , (e)  $L/a_x = 2.63 \pm 0.31$  and (f)  $L/a_x = 2.97 \pm 0.35$ . Here  $a_x \approx 21.0$  nm and  $d/a_x \approx 1.0$ .

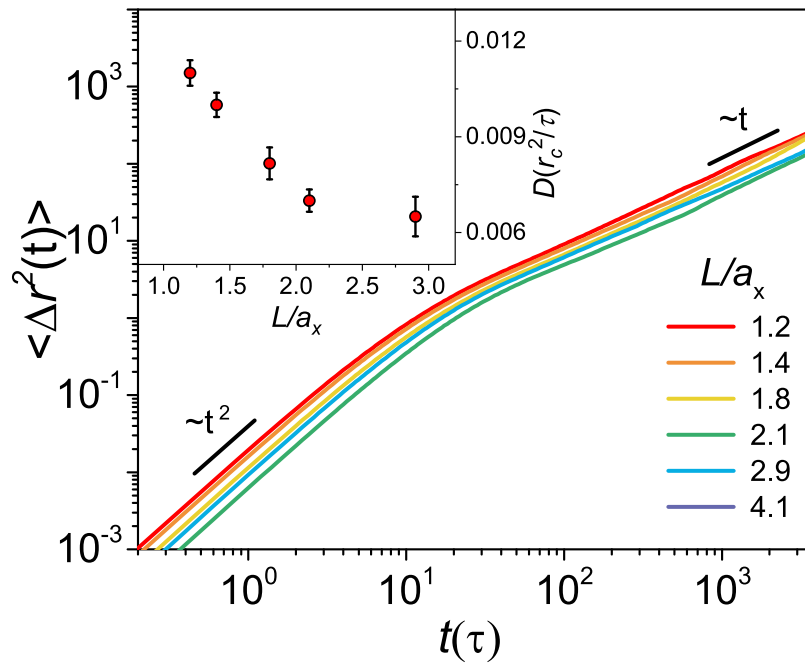


FIG. S5. The mean square displacement  $\langle \Delta r^2(t) \rangle$  and diffusion coefficient  $D$  (inset) for different  $L/a_x$  of the thin rods with  $d/a_x = 0.2$ .

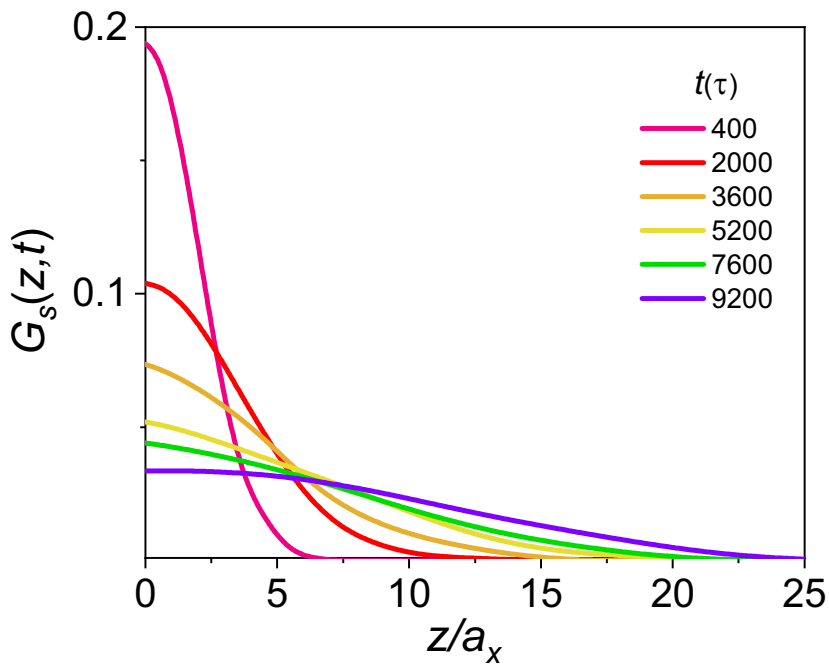


FIG. S6. The displacement probability distribution function  $G_s(z,t)$  of Brownian motion.

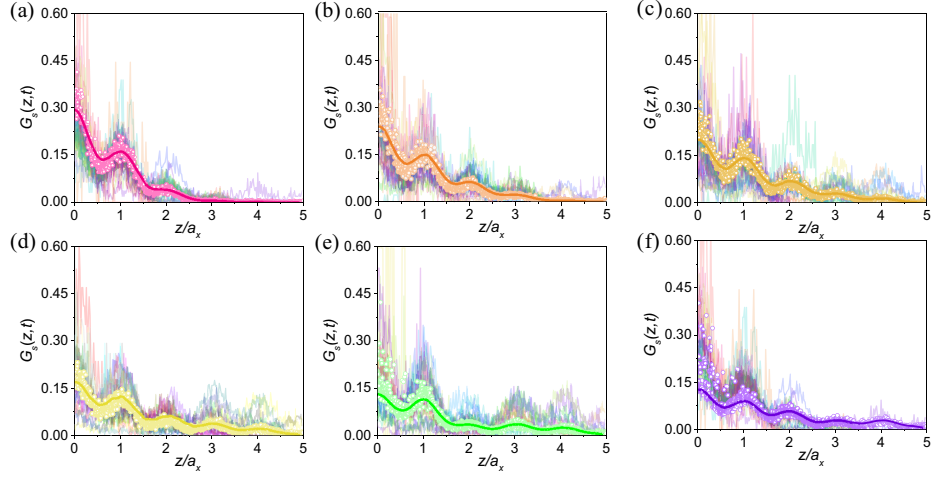


FIG. S7. The DPDFs obtained directly from the experimental measurements (half-transparent colored lines), the ensemble-averaged DPDFs (colored circles) and the smoothed lines for these circles (colored thick lines) of experimental  $G_s(z, t)$  of rods with  $L/a_x = 2.51 \pm 0.27$  at different times: (a) 220s (b) 380s (c) 500s (d) 650s (e) 750s and (f) 900s. The color of the half-transparent lines marks different particles.

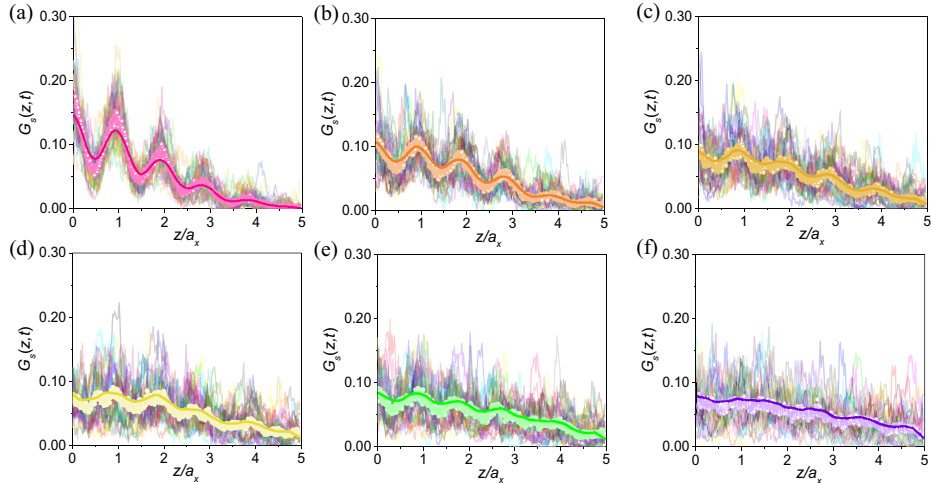


FIG. S8. The DPDFs obtained directly from the experimental measurements (half-transparent colored lines), the ensemble-averaged DPDFs (colored circles) and the smoothed lines for these circles (colored thick lines) of experimental  $G_s(z, t)$  of rods with  $L/a_x = 2.97 \pm 0.35$  at different times: (a) 220s (b) 380s (c) 500s (d) 650s (e) 750s and (f) 900s. The color of the half-transparent lines marks different particles.

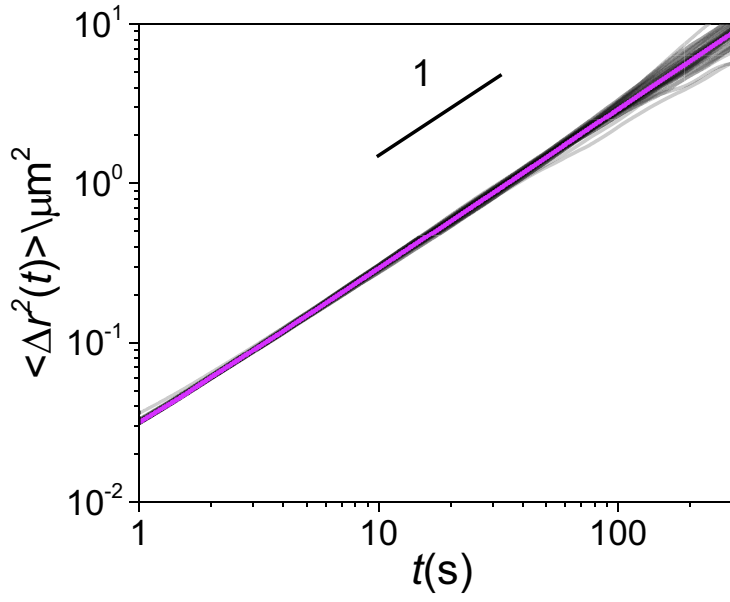


FIG. S9. Time-averaged  $\langle r^2(t) \rangle$  (gray lines), ensemble-averaged  $\langle r^2(t) \rangle$  for 10800s (magenta line) plotted against time on the log–log scale, where  $d/a_x = 1.0$  and  $L/a_x = 2.0$ .

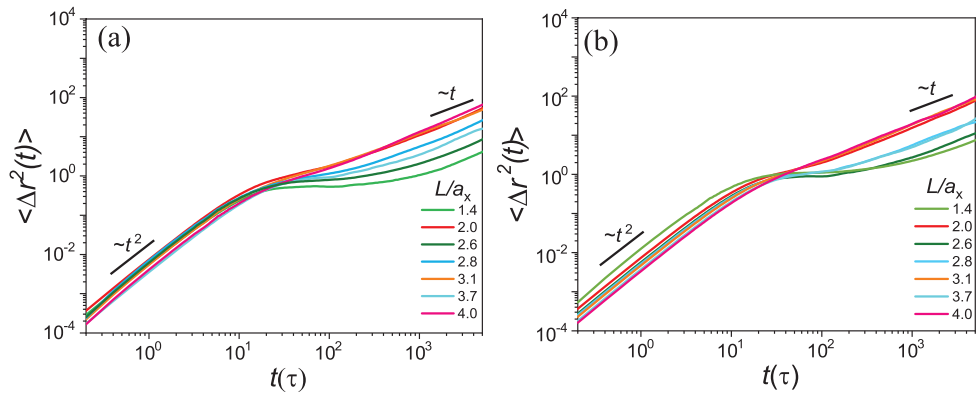


FIG. S10.  $\langle \Delta r^2(t) \rangle$  for different  $L/a_x$  at  $d/a_x = 1.4$ . (a)  $a_{ij} = 20$ , (b)  $a_{ij} = 30$ .

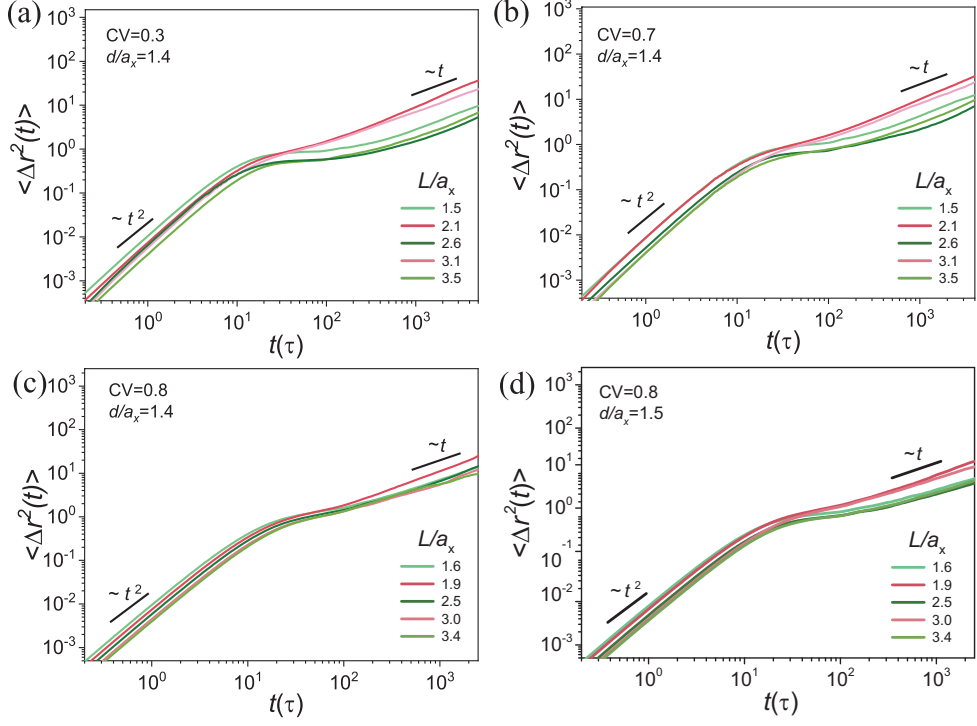


FIG. S11.  $\langle \Delta r^2(t) \rangle$  for different  $L/a_x$  at (a)  $d/a_x = 1.4$ ,  $CV=0.3$ , (b)  $d/a_x = 1.4$ ,  $CV=0.7$ , (c)  $d/a_x = 1.4$ ,  $CV =0.8$ , and (d)  $d/a_x = 1.5$ ,  $CV=0.8$ .

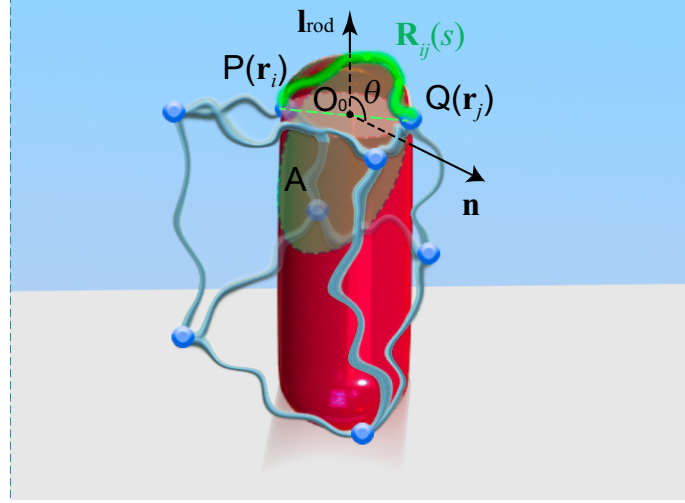


FIG. S12. Schematic of the deformation of network strands in contact with a rod, where the path of the strand  $\mathbf{R}_{ij}(s)$  is colored by green curve and the translucent green plane represents the  $A$  plane which is an osculating plane (with the normal vector  $\mathbf{n}$ ) passing through the cross-links  $P$  and  $Q$  with positional vectors  $\mathbf{r}_i$  and  $\mathbf{r}_j$ .

TABLE S1. Some recent demonstrations of various bacteria in different mucus.

Mucus	$a_x$	Bacterium	$d$	$d/a_x$	Reference
Colonic mucus	255nm	<i>Escherichia Coli</i>	250-500nm	1.0-1.9	[47, 51]
Intestinal mucus	240nm	<i>Vibrio cholerae</i>	500-800nm	2.1-3.3	[48, 52]
Porcine gastric mucin	525nm	rod-shaped <i>H. pylori</i>	500-1000nm	0.95-1.9	[50]
Gastric mucin	250nm	helical-shaped <i>H. pylori</i>	500nm	2.0	[49, 53]
Airway mucus	500nm	<i>Pseudomonas aeruginosa</i>	500-1000nm	1.0-2.0	[43, 54]
Airway mucus	500nm	<i>M. Tuberculosis</i>	500nm	1.0	[42, 55]
Airway mucus	500nm	<i>Porphyromonas</i>	500-800nm	1.0-1.6	[41]
Airway mucus	500nm	<i>Haemophilus influenzae</i>	300nm	0.60	[45, 56]
Airway mucus	500nm	<i>Escherichia Coli</i>	250-500nm	0.5-1.0	[46, 51]
Airway mucus	500nm	<i>Acinetobacter</i>	900nm	1.8	[44, 48, 57]
Cow cervical mucus	900nm	<i>Bacillus subtilis</i>	900nm	1.0	[28, 58]

TABLE S2. Average and standard error of lengths and diameters of Au-NRs in experiments.

Sample ID	01	02	03	04	05	06
Length(nm)	30.6 ± 3.4	42.7 ± 3.9	45.3 ± 4.9	52.5 ± 5.6	55.8 ± 6.7	61.4 ± 7.7
Diameter(nm)	18.2 ± 1.3	18.7 ± 0.9	19.7 ± 2.2	19.6 ± 1.7	19.9 ± 1.1	18.3 ± 1.9

TABLE S3. Storage modulus, loss modulus and mesh size for prepared hydrogels

Sample	Storage Modulus	Loss Modulus	Modulus	Mesh size
ID#	$G'$ (kPa)	$G'$ (kPa)	$G^*$ (kPa)	$\langle \xi \rangle_G$ (nm)
1	0.40	0.18	0.44	23.9
2	0.59	0.12	0.61	20.2
3	0.63	0.12	0.64	19.8
4	0.58	0.09	0.59	21.4
5	0.64	0.04	0.64	19.5
		Average	0.58 ± 0.08	21.0 ± 1.8

---

\* jianglx@scut.edu.cn

† ltyan@mail.tsinghua.edu.cn

‡ X. Z., X. D., and M. A. H. contributed equally.

- [1] J. M. Harris and R. B. Chess, *Nat. Rev. Drug Discov.* **2**, 214 (2003).
- [2] V. Hagel, T. Haraszti, and H. Boehm, *Biointerphases* **8**, 36 (2013).
- [3] T. Canal and N. A. Peppas, *J. Biomed. Mater. Res.* **23**, 1183 (1989).
- [4] M. S. Rehmann, K. M. Skeens, P. M. Kharkar, E. M. Ford, E. Maverakis, K. H. Lee, and A. M. Kloxin, *Biomacromolecules* **18**, 3131 (2017).
- [5] E. A. Phelps, N. O. Enemchukwu, V. F. Fiore, J. C. Sy, N. Murthy, T. A. Sulchek, T. H. Barker, and A. J. García, *Adv. Mater.* **24**, 64 (2012).
- [6] J. Lou and D. J. Mooney, *Nat. Rev. Chem.* **6**, 726 (2022).
- [7] C. A. Chazot, S. Nagelberg, C. J. Rowlands, M. R. Scherer, I. Coropceanu, K. Broderick, Y. Kim, M. G. Bawendi, P. T. So, and M. Kolle, *Nat. Photon.* **14**, 310 (2020).
- [8] Y. Park, S. Shin, H. Jin, J. Park, Y. Hong, J. Choi, B. Jung, H. Song, and D. Seo, *J. Am. Chem. Soc.* **140**, 15161 (2018).
- [9] I. Y. Wong, M. L. Gardel, D. R. Reichman, E. R. Weeks, M. T. Valentine, A. R. Bausch, and D. A. Weitz, *Phys. Rev. Lett.* **92**, 178101 (2004).
- [10] D. B. Allan, T. Caswell, N. C. Keim, C. M. van der Wel, and R. W. Verweij, *soft-matter/trackpy: Trackpy v0.5.0* (Zenodo, 2021).
- [11] J. Schindelin, I. Arganda-Carreras, E. Frise, V. Kaynig, M. Longair, T. Pietzsch, S. Preibisch, C. Rueden, S. Saalfeld, B. Schmid, *et al.*, *Nat. Methods* **9**, 676 (2012).
- [12] J. C. Crocker and D. G. Grier, *J. Colloid Interface Sci.* **179**, 298 (1996).
- [13] B. S. Schuster, L. M. Ensign, D. B. Allan, J. S. Suk, and J. Hanes, Particle tracking in drug and gene delivery research: State-of-the-art applications and methods, *Adv. Drug Deliver. Rev.* **91**, 70 (2015).
- [14] M. Lindén, V. Ćurić, E. Amselem, and J. Elf, Pointwise error estimates in localization microscopy, *Nat. Commun.* **8**, 15115 (2017).
- [15] K. M. Spillane, J. Ortega-Arroyo, G. De Wit, C. Eggeling, H. Ewers, M. I. Wallace, and P. Kukura, High-speed single-particle tracking of gm1 in model membranes reveals anomalous

- diffusion due to interleaflet coupling and molecular pinning, *Nano Lett.* **14**, 5390 (2014).
- [16] R. D. Groot and P. B. Warren, *J. Chem. Phys.* **107**, 4423 (1997).
  - [17] X. Yong, O. Kuksenok, K. Matyjaszewski, and A. C. Balazs, *Nano Lett.* **13**, 6269 (2013).
  - [18] G. Raos and M. Casalegno, *J. Chem. Phys.* **134**, 054902 (2011).
  - [19] Z. Xu, X. Dai, X. Bu, Y. Yang, X. Zhang, X. Man, X. Zhang, M. Doi, and L.-T. Yan, *ACS Nano* **15**, 4608 (2021).
  - [20] H. Tanaka, *Phys. Rev. Lett.* **71**, 3158 (1993).
  - [21] P.-O. Persson and G. Strang, *SIAM Rev.* **46**, 329 (2004).
  - [22] T. Miller Iii, M. Eleftheriou, P. Pattnaik, A. Ndirango, D. Newns, and G. Martyna, *J. Chem. Phys.* **116**, 8649 (2002).
  - [23] K. Yang and Y.-Q. Ma, *Nat. Nanotechnol.* **5**, 579 (2010).
  - [24] M. Calvaresi, M. Dallavalle, and F. Zerbetto, *Small* **5**, 2191 (2009).
  - [25] M. Yu, J. Wang, Y. Yang, C. Zhu, Q. Su, S. Guo, J. Sun, Y. Gan, X. Shi, and H. Gao, *Nano Lett.* **16**, 7176 (2016).
  - [26] T. Fischer, A. Hayn, and C. T. Mierke, *Sci. Rep.* **9**, 1 (2019).
  - [27] S. K. Lai, Y.-Y. Wang, K. Hida, R. Cone, and J. Hanes, *Proc. Natl. Acad. Sci. U.S.A.* **107**, 598 (2010).
  - [28] N. Figueroa-Morales, L. Dominguez-Rubio, T. L. Ott, and I. S. Aranson, *Sci. Rep.* **9**, 9713 (2019).
  - [29] R. Deam and S. F. Edwards, *Phys. Trans. R. Soc.* **280**, 317 (1976).
  - [30] F. Schmid, *Phys. Rev. Lett.* **111**, 028303 (2013).
  - [31] R. L. Graham, *Info. Pro. Lett.* **1**, 132 (1972).
  - [32] E. W. Montroll and G. H. Weiss, *J. Math. Phys.* **6**, 167 (1965).
  - [33] R. Metzler and J. Klafter, *Phys. Rep.* **339**, 1 (2000).
  - [34] A. E. Cohen, *Phys. Rev. Lett.* **94**, 118102 (2005).
  - [35] V. Mel'nikov, *Phys. Rep.* **209**, 1 (1991).
  - [36] A. Dechant, F. Kindermann, A. Widera, and E. Lutz, *Phys. Rev. Lett.* **123**, 070602 (2019).
  - [37] J. Slezak and S. Burov, *Sci. Rep.* **11**, 5101 (2021).
  - [38] M. Smith, R. Poling-Skutvik, A. H. Slim, R. C. Willson, and J. C. Conrad, *Macromolecules* **54**, 4557 (2021).
  - [39] S. Alam and A. Mukhopadhyay, *Macromolecules* **47**, 6919 (2014).

- [40] R. Poling-Skutvik, R. Krishnamoorti, and J. C. Conrad, ACS Macro Lett. **4**, 1169 (2015).
- [41] J. Durack, S. Lynch, S. Nariya, N. Bhakta, M. Castro, A.-M. Dyer, E. Israel, M. Kraft, R. Martin, D. Mauger, S. Rosenberg, T. Sharp-King, S. White, P. Woodruff, P. Avila, L. Denlinger, F. Holguin, S. Lazarus, and Y. Huang, J. Allergy Clin. Immunol. **140**, 63–75 (2017).
- [42] S. Vijay, H. T. Hai, D. D. A. Thu, E. Johnson, A. Pielach, N. H. Phu, G. E. Thwaites, and N. T. T. Thuong, Front. Microbiol. **8**, 2681 (2018).
- [43] G. A. Duncan, J. Jung, A. Joseph, A. L. Thaxton, N. E. West, M. P. Boyle, J. Hanes, and J. S. Suk, JCI Insight. **1**, e88198 (2016).
- [44] K. Yamada, Y. Morinaga, K. Yanagihara, N. Kaku, Y. Harada, N. Uno, S. Nakamura, Y. Ima-mur, H. Hasegawa, T. Miyazaki, K. Izumikawa, H. Kakeya, H. Mikamo, and S. Kohno, Pulm. Pharmacol. Ther. **28**, 165 (2014).
- [45] J. V. Fahy and B. F. Dickey, N. Engl. J. Med. **363**, 2233 (2010).
- [46] H. Matsui, M. W. Verghese, M. Kesimer, U. E. Schwab, S. H. Randell, J. K. Sheehan, B. R. Grubb, and R. C. Boucher, J. Immunol. **175**, 1090 (2005).
- [47] H. M. Yildiz, T. L. Carlson, A. M. Goldstein, and R. L. Carrier, Macromol. Biosci. **15**, 712 (2015).
- [48] N. T. Q. Nhu, J. S. Lee, H. J. Wang, and Y. S. Dufour, J. Bacteriol. **203**, e00607 (2021).
- [49] T. Pelaseyed, J. H. Bergström, J. K. Gustafsson, A. Ermund, G. M. Birchenough, A. Schütte, S. van der Post, F. Svensson, A. M. Rodríguez-Piñeiro, E. E. Nyström, C. Wising, M. E. V. Johansson, and G. C. Hansson, Immunol. Rev. **260**, 8 (2014).
- [50] M. A. Constantino, M. Jabbarzadeh, H. C. Fu, and R. Bansil, Sci. Adv. **2**, e1601661 (2016).
- [51] M. Riley, *Size limits of very small microorganisms: proceedings of a workshop* (National Academies Press Washington DC, 1999).
- [52] D. E. Blue and S. D. Allen, *Essentials of anatomic pathology* (Springer, 2011).
- [53] R. Bansil, J. P. Celli, J. M. Hardcastle, and B. S. Turner., Front. Immunol. **4**, 310 (2013).
- [54] S. P. Diggle and M. Whiteley, Microbio. **166**, 30 (2020).
- [55] S. L. Percival and D. W. Williams, *Microbiology of waterborne diseases* (Elsevier, 2014).
- [56] S. H. Gabriel Waksman, Michael Caparon, *Structural Biology of Bacterial Pathogenesis* (ASM Press, 2006).
- [57] C. de W Blackburn, *Food spoilage microorganisms* (Woodhead Publishing, 2006).
- [58] R. G. Leuschner, D. P. Ferdinando, and P. J. Lillford, Colloids Surf. B **19**, 31 (2000).